SCIE 4500 Final Report: A Study on Cosmological Parity Violation

K. Yue[1, *]

[1]*Department of Physics, The Hong Kong University of Science and Technology, Hong Kong S.A.R., P.R.China*
(Dated: May 10, 2024)

If parity violation exists in the early universe, it can leave detectable traces for cosmological observation at later times. One notable example is the primordial scalar four-point correlation function (4PCF). This paper explores the possibility that cosmological parity violations originate from the coupling between a massive spin-1 field and a Goldstone boson, which resulted from broken time translations during inflation [1]. By adopting an effective field theory (EFT) approach, the interaction action can be described non-locally, and the magnitude of parity-odd signals on the trispectrum is estimated. Furthermore, two independent research teams have reported compelling evidence for parity violation [2 and 3]. To validate their findings, Python codes capable of computing the parity-odd signals derived from the 4PCF of the Baryon Oscillation Spectroscopic Survey (BOSS) have been developed. The codes have undergone thorough testing using a toy model, and the 4PCF estimator for angular momentum multipoles (1, 1, 1) and (1, 2, 2) has been computed using a sample of 1000 galaxies from the BOSS CMASS dataset.

I. INTRODUCTION

The search for parity violation has a long history and remains an active research topic. In the Standard Model (SM), the weak interaction is the only fundamental force violating parity [4], and it played no role in the evolution of the large-scale distribution of matter. Any observation of a cosmological parity violation would therefore imply the existence of a new CP-violating force at inflation. Such a parity-violating force might even be able to explain the observed baryon asymmetry, as envisaged by the Sakharov conditions [5]. The detection of a parity violation in cosmological observations would be a significant discovery, providing evidence for physics beyond the SM.
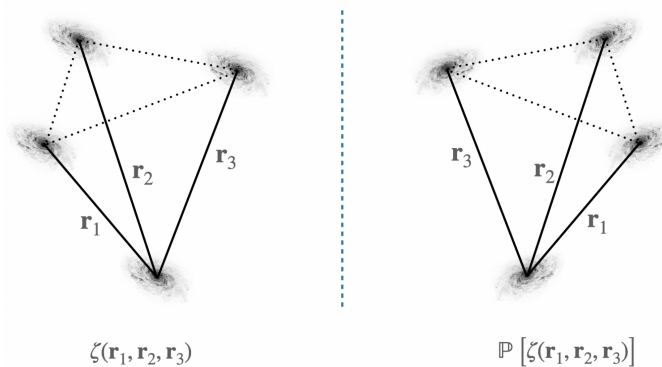

FIG. 1: At least four non-planar points are required to establish chirality. [2]

To test for parity violation, parity-sensitive observables are required. Due to their coplanar topology, the galaxy's isotropic two-point or three-point correlation functions (2PCF or 3PCF) are insensitive to parity. More generally, in a D-dimensional space, the N-point correlation function (NPCF) is sensitive to parity only if $N > D$ [6]. Since our universe is three-dimensional (3D), the simplest statistic to study scalar parity violation in large-scale structure (LSS) surveys is the 4PCF [7 and 8]. The 4PCF's sensitivity to parity can also be intuitively understood by the fact that at least four non-planar points are required to establish chirality, i.e., $\zeta(\vec{r}_1, \vec{r}_2, \vec{r}_3) \neq \mathbb{P}[\zeta(\vec{r}_1, \vec{r}_2, \vec{r}_3)]$, as shown in FIG. 1 [2].

This project focuses on two main objectives. The first objective is to study the physics associated with the coupling between a massive spin-1 field and a Goldstone boson during inflation. In tree-level cosmological correlators for single-field inflation, parity violation is prohibited [9 and 10]. However, by introducing additional massive particles in the primordial universe, this restriction can be bypassed to produce a parity-violating signal in the trispectrum. Another objective of this project is to validate the findings presented in [2] and [3]. In the study by [2], the authors conducted a blind test for parity violation in the 4PCF using the Baryon Oscillation Spectroscopic Survey (BOSS) CMASS sample. A non-parametric rank test and a compressed-χ^2 analysis are employed to analyze the data. The rank test yielded a detection significance of 2.9σ. A similar analysis was carried out in [3], which reported a significance of 3.1σ in LOWZ and a significantly higher significance of 7.1σ in CMASS.

The remaining work is structured as follows. §II provides an overview of the theoretical concepts, including the 4PCF estimator, the necessary corrections to account for non-uniform geometry, and the interplay between the massive spin-1 field and the Goldstone boson. §III delves into the effective field theory (EFT) approach for the interaction action. It discusses the estimated size of parity-odd signals induced on the trispectrum, the parity-odd trispectrum at the leading-order (LO), and its shape characteristics. In §IV, the measurement of the parity-odd 4PCF using toy tetrahedra is illustrated. §V presents the results of measuring the

* ckkyue@connect.ust.hk

parity-odd 4PCF using a test sample from the Sloan Digital Sky Survey-III (SDSS-III) [11], which consists of 1000 galaxies. The limitations of the coding and systematic uncertainties are discussed in §VI. Finally, §VII concludes the work. Python codes of our analysis work can be found on https://github.com/ckkyue/4PCF.

II.   THEORETICAL BACKGROUND

A.   Parity-Odd Component of 4PCF

The primordial fluctuations observed in modern cosmological surveys are generated by the quantum fluctuation of the inflaton field, represented as $\phi = \phi_0 + \varphi$. Here, ϕ_0 and φ represent the background field and its fluctuations, respectively. The Fourier modes of the inflaton field have the solution [12]

$$\varphi(\tau, \vec{k}) = \frac{H}{\sqrt{2k^3}}(1 + ik\tau)e^{-ik\tau}, \qquad (1)$$

where τ is the conformal time defined as $d\tau \equiv \frac{dt}{a}$. Using the spatial flat gauge $\zeta = -\frac{H}{\dot{\phi}_0}\varphi$, the inflaton fluctuation given by eq. (1) can be translated into curvature fluctuation ζ. Expanding in the Fourier space,

$$\zeta(t, \vec{x}) = \int \frac{d^3k}{(2\pi)^3}\zeta(t, \vec{k})e^{i\vec{k}\cdot\vec{x}}. \qquad (2)$$

Since $\zeta(t, \vec{x})$ is real, for each k-mode we have $\zeta^*(t, \vec{k}) = \zeta(t, -\vec{k})$. Under parity transformation, the NPCF transforms according to

$$\langle\Pi_i^n\zeta(t, \vec{k}_i)\rangle \xrightarrow{\mathbb{P}} \langle\Pi_i^n\zeta(t, -\vec{k}_i)\rangle = \langle\Pi_i^n\zeta(t, \vec{k}_i)\rangle^*. \qquad (3)$$

This proves parity violation in the 4PCF manifests itself as a parity-odd imaginary component.

B.   4PCF Estimator

The fractional density fluctuation is $\delta(\vec{x}) \equiv \frac{\rho(\vec{x})}{\bar{\rho}} - 1$, where $\bar{\rho}$ is the average density, and $\rho(\vec{x})$ is the density field at some location $\vec{x}$ away from the origin. The Planck and Wilkinson Microwave Anisotropy Probe (WMAP) results have provided the most stringent limits on the non-Gaussianity of the distribution of density fluctuations in the early universe [13 and 14].

The 4PCF is a measure of the correlation between four points in space. It quantifies the excessive tendency of groups of four galaxies to cluster together compared to random distribution, and is mathematically defined as

$$\hat{\zeta}(\vec{r}_1, \vec{r}_2, \vec{r}_3) \equiv \langle\delta(\vec{x})\delta(\vec{x}+\vec{r}_1)(\vec{x}+\vec{r}_2)(\vec{x}+\vec{r}_3)\rangle, \qquad (4)$$

where $\langle\rangle$ indicates an ensemble average of the density

fluctuation field. Applying the ergodic principle, the ensemble average can be replaced by an integral of spatial position $\vec{x}$ over the volume V of the survey, rewriting eq. (4) into

$$\hat{\zeta}(\vec{r}_1, \vec{r}_2, \vec{r}_3) = \frac{1}{V}\int d\vec{x}\delta(\vec{x})\delta(\vec{x}+\vec{r}_1)(\vec{x}+\vec{r}_2)(\vec{x}+\vec{r}_3). \qquad (5)$$

The 4PCF estimated from cosmological survey follows:

$$\hat{\zeta}(\vec{r}_1, \vec{r}_2, \vec{r}_3) = \frac{1}{V}\int_{\vec{r}_1,\vec{r}_2,\vec{r}_3\in\text{bins}} d\vec{x}\delta(\vec{x}) \\ \times \delta(\vec{x}+\vec{r}_1)\delta(\vec{x}+\vec{r}_2)\delta(\vec{x}+\vec{r}_3), \qquad (6)$$

which we have included the finite-size radial bins. As a remark, we choose $r_1 < r_2 < r_3$ to avoid over-counting the tetrahedra. Eq. (6) implies measuring the 4PCF requires counting of quadruplets of galaxies (see FIG. 2 [15]), and the computational complexity $\sim \mathcal{O}(N_g^4)$ with N_g being the number of galaxies. Considering the substantial number of galaxies, approximately 10^6, in the BOSS CMASS sample [16], it is imperative to advance our algorithm to finish the computation within a reasonable amount of time. In the following, a method that reduces the complexity to $\mathcal{O}(N_g^2)$ is outlined.
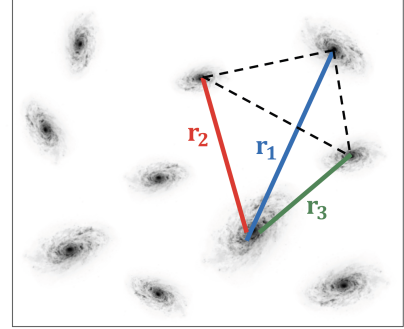

FIG. 2: A quadruplet of galaxies. Three vectors $\vec{r}_1$, $\vec{r}_2$, and $\vec{r}_3$ extend from the galaxy corresponding to primary vertex. [15]

Ignoring redshift space distortions, the 3D distribution of galaxies is assumed to be isotropic on cosmological scales, which means it remains invariant under simultaneous rotations of all coordinates. The isotropic basis is hence an efficient method to extract cosmological information systematically. Expanding the 4PCF in the basis of isotropic functions [2],

$$\hat{\zeta}(\vec{r}_1, \vec{r}_2, \vec{r}_3) = \sum_{l_1l_2l_3} \hat{\zeta}_{l_1l_2l_3}(r_1, r_2, r_3)\mathcal{P}_{l_1l_2l_3}(\hat{\vec{r}}_1, \hat{\vec{r}}_2, \hat{\vec{r}}_3). \qquad (7)$$

The first part of eq. (7) is the coefficients, and the second part is the isotropic basis functions [16], which can be

decomposed into spherical harmonics as

$$
\mathcal{P}_{l_1 l_2 l_3}(\hat{\vec{r}}_1, \hat{\vec{r}}_2, \hat{\vec{r}}_3) \equiv (-1)^{l_1+l_2+l_3} \sum_{m_1 m_2 m_3} \begin{pmatrix} l_1 & l_2 & l_3 \\ m_1 & m_2 & m_3 \end{pmatrix}
$$
$$
\times Y_{l_1 m_1}(\hat{\vec{r}}_1) Y_{l_2 m_2}(\hat{\vec{r}}_2) Y_{l_3 m_3}(\hat{\vec{r}}_3),
\tag{8}
$$

which the Wigner 3-j symbol

$$
\begin{pmatrix} l_1 & l_2 & l_3 \\ m_1 & m_2 & m_3 \end{pmatrix} \equiv \frac{(-1)^{l_1-l_2-m_3}}{\sqrt{2l_3+1}} \langle l_1 m_1 l_2 m_2 | l_3 (-m_3) \rangle
\tag{9}
$$

is included, and the summation includes $m_i \in [-l_i, l_i]$.

We first demonstrate the rotational invariance of the isotropic basis functions. The isotropy of these functions implies they are independent of specific components along any axis, i.e., $\sum_{i=1}^{3} m_i = 0$. This condition is automatically satisfied, since the Clebsch–Gordan (CG) coefficient $\langle l_1 m_1 l_2 m_2 | l_3 (-m_3) \rangle$ in the Wigner 3-j symbol is non-zero only if $\sum_{i=1}^{3} m_i = 0$. Moreover, these basis functions are orthonormal to each other:

$$
\int d\hat{\vec{r}}_1 d\hat{\vec{r}}_2 d\hat{\vec{r}}_3 \mathcal{P}_{l_1 l_2 l_3}(\hat{\vec{r}}_1, \hat{\vec{r}}_2, \hat{\vec{r}}_3) \times \mathcal{P}^*_{l'_1 l'_2 l'_3}(\hat{\vec{r}}_1, \hat{\vec{r}}_2, \hat{\vec{r}}_3)
$$
$$
= \delta_{l_1 l'_1} \delta_{l_2 l'_2} \delta_{l_3 l'_3}.
\tag{10}
$$

Next, we show the coefficients part in eq. (7) is separable in r_i. Consider the integral

$$
\int d\hat{\vec{r}}_1 d\hat{\vec{r}}_2 d\hat{\vec{r}}_3 \mathcal{P}^*_{l_1 l_2 l_3}(\hat{\vec{r}}_1, \hat{\vec{r}}_2, \hat{\vec{r}}_3) \hat{\zeta}(\hat{\vec{r}}_1, \hat{\vec{r}}_2, \hat{\vec{r}}_3)
$$
$$
= \int d\hat{\vec{r}}_1 d\hat{\vec{r}}_2 d\hat{\vec{r}}_3 \mathcal{P}^*_{l_1 l_2 l_3}(\hat{\vec{r}}_1, \hat{\vec{r}}_2, \hat{\vec{r}}_3)
$$
$$
\times \sum_{l'_1 l'_2 l'_3} \hat{\zeta}_{l'_1 l'_2 l'_3}(r_1, r_2, r_3) \mathcal{P}_{l'_1 l'_2 l'_3}(\hat{\vec{r}}_1, \hat{\vec{r}}_2, \hat{\vec{r}}_3)
$$
$$
= \sum_{l'_1 l'_2 l'_3} \int d\hat{\vec{r}}_1 d\hat{\vec{r}}_2 d\hat{\vec{r}}_3 \mathcal{P}^*_{l_1 l_2 l_3}(\hat{\vec{r}}_1, \hat{\vec{r}}_2, \hat{\vec{r}}_3)
$$
$$
\times \mathcal{P}_{l'_1 l'_2 l'_3}(\hat{\vec{r}}_1, \hat{\vec{r}}_2, \hat{\vec{r}}_3) \hat{\zeta}_{l'_1 l'_2 l'_3}(r_1, r_2, r_3)
$$
$$
= \hat{\zeta}_{l_1 l_2 l_3}(r_1, r_2, r_3),
\tag{11}
$$

where we have applied the orthonormal relation given in eq. (10) to arrive at the last line. Define harmonic coefficients as

$$
a_{lm}(x; \vec{r}_i) \equiv \int d\hat{\vec{r}}_i \delta(\vec{x} + \vec{r}_i) Y_{lm}(\hat{\vec{r}}_i),
\tag{12}
$$

eq. (11) turns into

$$
\hat{\zeta}_{l_1 l_2 l_3}(r_1, r_2, r_3)
$$
$$
= \int d\hat{\vec{r}}_1 d\hat{\vec{r}}_2 d\hat{\vec{r}}_3 \sum_{m_1 m_2 m_3} \begin{pmatrix} l_1 & l_2 & l_3 \\ m_1 & m_2 & m_3 \end{pmatrix}
$$
$$
\times Y_{l_1 m_1}(\hat{\vec{r}}_1) Y_{l_2 m_2}(\hat{\vec{r}}_2) Y_{l_3 m_3}(\hat{\vec{r}}_3)
$$

$$
\times \frac{1}{V} \int d\vec{x} d\hat{\vec{r}}_1 d\hat{\vec{r}}_2 d\hat{\vec{r}}_3 \delta(\vec{x}) \delta(\vec{x}+\vec{r}_1) \delta(\vec{x}+\vec{r}_2) \delta(\vec{x}+\vec{r}_3)
$$
$$
= \frac{1}{V} \sum_{m_1 m_2 m_3} \begin{pmatrix} l_1 & l_2 & l_3 \\ m_1 & m_2 & m_3 \end{pmatrix}
$$
$$
\times \int d\vec{x} d\hat{\vec{r}}_1 d\hat{\vec{r}}_2 d\hat{\vec{r}}_3 \delta(\vec{x}) \delta(\vec{x}+\vec{r}_1) \delta(\vec{x}+\vec{r}_2) \delta(\vec{x}+\vec{r}_3)
$$
$$
\times Y_{l_1 m_1}(\hat{\vec{r}}_1) Y_{l_2 m_2}(\hat{\vec{r}}_2) Y_{l_3 m_3}(\hat{\vec{r}}_3)
$$
$$
= \frac{1}{V} \sum_{m_1 m_2 m_3} \begin{pmatrix} l_1 & l_2 & l_3 \\ m_1 & m_2 & m_3 \end{pmatrix} \int d\vec{x} \delta(\vec{x}) \prod_{i=1}^{3} a_{l_i m_i}(\vec{x}; r_i).
\tag{13}
$$

Using eq. (13), the computational complexity of the 4PCF estimator is reduced to $\mathcal{O}(N_g^2)$.

C. Edge-Correction

To mitigate the effects of non-uniform survey geometry, the 4PCF estimator in eq. (13) needs to be modified to the generalized Landy-Szalay form [17 and 18]:

$$
\hat{\zeta}(\vec{r}_1, \vec{r}_2, \vec{r}_3) = \frac{\mathcal{N}(\vec{r}_1, \vec{r}_2, \vec{r}_3)}{\mathcal{R}(\vec{r}_1, \vec{r}_2, \vec{r}_3)}.
\tag{14}
$$

Here, $\mathcal{N}$ and $\mathcal{R}$ are the 4PCF estimates obtained from "data-minus-random" and random catalogs, respectively. The edge-corrected 4PCF multiplets are then given by

$$
\hat{\zeta}_{l_1 l_2 l_3}(r_1, r_2, r_3) = \sum_{l'_1 l'_2 l'_3} [M^{-1}]^{l'_1 l'_2 l'_3}_{l_1 l_2 l_3}(r_1, r_2, r_3)
$$
$$
\times \frac{\mathcal{N}_{l'_1 l'_2 l'_3}(r_1, r_2, r_3)}{\mathcal{R}_{000}(r_1, r_2, r_3)},
\tag{15}
$$

in which the coupling matrix is defined as

$$
M^{l'_1 l'_2 l'_3}_{l_1 l_2 l_3}(r_1, r_2, r_3) = \frac{(-1)^{l'_1+l'_2+l'_3}}{(4\pi)^{\frac{3}{2}}} \times \sum_{L_1 L_2 L_3} \frac{\mathcal{R}_{L_1 L_2 L_3}(r_1, r_2, r_3)}{\mathcal{R}_{000}(r_1, r_2, r_3)}
$$
$$
\left[\prod_{i=1}^{3} \sqrt{(2l_i+1)(2L_i+1)(2l'_i+1)} \right] \begin{Bmatrix} l_1 & L_1 & l'_1 \\ l_2 & L_2 & l'_2 \\ l_3 & L_3 & l'_3 \end{Bmatrix}
$$
$$
\times \begin{pmatrix} l_1 & L_1 & l'_1 \\ 0 & 0 & 0 \end{pmatrix} \begin{pmatrix} l_2 & L_2 & l'_2 \\ 0 & 0 & 0 \end{pmatrix} \begin{pmatrix} l_3 & L_3 & l'_3 \\ 0 & 0 & 0 \end{pmatrix},
\tag{16}
$$

and the curly bracket denotes the Wigner 9-j symbol.

To sum up, the 4PCF is first expanded in the basis of isotropic functions, enabling us to separate the coefficients into decoupled integrals. By doing so, the estimator is factorized into independent components corresponding to pairs of galaxies. This factorization significantly reduces the computational complexity to $\mathcal{O}(N_g^2)$, facilitating the calculation of the 4PCF for galaxy surveys in a feasible manner.

In the first half of §II, the concepts and equations pre-

sented allow us to construct the Python codes for computing the parity-odd signals from a galaxies sample. The subsequent discussion focuses on the possible origin of parity violation by examining the coupling between a massive spin-1 field and a Goldstone boson.

D. Massive Spin-1 Field

A potential source of parity violation arises from the presence of a massive spin-1 field with a parity-breaking chemical potential. The action of the dynamics is given by [1 and 19]:

$$S = \int d^4x \sqrt{-g} \left[-\frac{1}{4} F_{\mu\nu} F^{\mu\nu} + \frac{1}{2} m_A^2 A_\mu A^\mu - \frac{\kappa t}{4} F_{\mu\nu} \tilde{F}^{\mu\nu} \right]. \tag{17}$$

Here, $F_{\mu\nu}$ represents the field strength of spin-1 field $\vec{A}$, $\tilde{F}^{\mu\nu} \equiv \frac{1}{2} \frac{\varepsilon^{\mu\nu\rho\sigma}}{\sqrt{-g}} F_{\rho\sigma}$ represents its Hodge dual, m_A is the mass of the vector boson, and κ is the chemical potential. The spacetime background is the four-dimensional (4D) de Sitter space with the metric

$$ds^2 \equiv g_{\mu\nu} dx^\mu dx^\nu = a^2(\tau)(d\tau^2 - dx_i dx^i). \tag{18}$$

The chemical potential originates from the dimension-5 coupling $\phi F_{\mu\nu} \tilde{F}^{\mu\nu}$ between the inflation field ϕ and vector field $\vec{A}$. Using slow-roll approximation, the inflaton field is expanded around ϕ_0 as $\phi \approx \phi_0 + \dot{\phi}_0 t$ with higher-order terms suppressed, e.g. $|\ddot{\phi}| \ll |3H\dot{\phi}|, |V_\phi|$. Since $\phi_0 F_{\mu\nu} \tilde{F}^{\mu\nu}$ only contributes a total derivative term, it can be disregarded in the action. The chemical potential is therefore given by $\kappa = \frac{\dot{\phi}_0}{\Lambda_\kappa}$, where Λ_κ is a cutoff energy scale.

Alternatively, eq. (17) can be rewritten as

$$S = \int d^4x \sqrt{-g} \left[-\frac{1}{4} F_{\mu\nu} F^{\mu\nu} + \frac{1}{2} m_A^2 A_\mu A^\mu \right.$$
$$\left. -\frac{1}{4\Lambda_\kappa} \phi F_{\mu\nu} \tilde{F}^{\mu\nu} \right]. \tag{19}$$

By varying the action in eq. (19) and adopting the covariant gauge $\partial_\mu(\sqrt{-g} A^\mu) = 0$, the equation of motion for the massive vector field is derived as (refer to Appendix A for more details)

$$\vec{A}'' - \nabla^2 \vec{A} - \frac{a\dot{\phi}_0}{\Lambda_\kappa} \nabla \times \vec{A} + a^2 m_A^2 \vec{A} = 0, \tag{20}$$

where the prime and dot notations denote differentiation with respect to the conformal time τ and proper time t, respectively. To solve eq. (20), we switch to the momentum space and decompose $\vec{A}(\tau, \vec{x})$ into its Fourier modes:

$$\vec{A}(\tau, \vec{x}) = \sum_{\lambda = 0, \pm} \int \frac{d^3k}{(2\pi)^{\frac{3}{2}}} \left[\vec{\varepsilon}_\lambda(\vec{k}) A_\lambda(\tau, \vec{k}) a_\lambda(\vec{k}) e^{i\vec{k}\cdot\vec{x}} + \text{h.c.} \right]. \tag{21}$$

Here, $\lambda = 0, \pm$ represent the longitudinal and transverse modes, $\vec{\varepsilon}_\lambda$ are the polarization vectors, and a_λ, $a_\lambda^\dagger$ are the annihilation and creation operators that satisfy the commutation relation:

$$\left[a_\lambda(\vec{k}), a_{\lambda'}^\dagger(\vec{k}') \right] = \delta_{\lambda\lambda'} \delta^3(\vec{k} - \vec{k}'). \tag{22}$$

Applying eq. (21) and decomposing the vector field into different helicity states, eq. (20) becomes

$$\begin{cases} A_\pm''(\tau, k) + (k^2 \pm 2a\kappa k + a^2 m_A^2) A_\pm(\tau, k) = 0, \\ A_0''(\tau, k) + (k^2 + a^2 m_A^2) A_0(\tau, k) = 0, \end{cases} \tag{23}$$

which the vector notation on $\vec{k}$ is dropped since the equations depend on its magnitude k only. From eq. (23), we notice the chemical potential affects the transverse modes but not the longitudinal one, as it appears solely in the equation of motion for $A_\pm$. The solution of the transverse modes is given by [1]

$$A_\pm = \frac{1}{\sqrt{2k}} e^{\mp \frac{\kappa}{2H}} W_{\frac{i\kappa}{H}, i\mu}(2ik\tau), \tag{24}$$

where W denotes the Whittaker function [20], and $\mu \equiv \sqrt{(m_A/H)^2 - \frac{1}{4}}$. The mass of the vector field is required to fulfill $m_A/H \geq \frac{1}{2}$ so that $\mu \in \mathbb{R}$.

The equation of motion of the transverse modes from eq. (23) can be rewritten as

$$\left[\left(\frac{\partial^2}{\partial t^2} + H \frac{\partial}{\partial t} \right) + \left(\frac{k^2}{a^2} \pm 2a\kappa \frac{k}{a} + m_A^2 \right) \right] A_\pm = 0, \tag{25}$$

which leads to the dispersion relation for physical momentum $k_p \equiv \frac{k}{a}$ by imposing $A \sim e^{i\omega t}$:

$$\omega_A^2 = (k_p \pm \kappa)^2 + m_A^2 - \kappa^2 - \frac{H^2}{4}. \tag{26}$$

Without loss of generality, consider the case $\kappa > 0$. For $\kappa > m_A$, the dispersion relation eq. (26) shows that A_- modes experience a tachyonic instability when $w_-^2(k_p) < 0$. This instability leads to an exponential enhancement of gauge boson production, which may damage the inflationary background. The analysis follows is therefore restricted to $\kappa \leq m$.

E. Goldstone Boson Action and Interactions

The Goldstone's theorem states that massless particles emerge when a continuous symmetry is spontaneously

broken [21]. In the context of the inflationary epoch, the vacuum expectation value of the background inflaton field breaks time-translations invariance. The fluctuations around this time-dependent background are described by the Goldstone boson π, which is associated with the process of symmetry breaking [22]. The Lagrangian for π is constructed using quantities that remain invariant under spatial diffeomorphism $x^i \rightarrow x^i + \xi^i(\vec{x}, t)$, such as g^{00}, $\partial_\mu g^{00}$, and the extrinsic curvature of constant time surfaces $K_{\mu\nu}$. The action takes the form [23]:

$$S_\pi = \int d^4x \sqrt{-g}\left[\frac{1}{2}M_{\rm Pl}^2 R + M_{\rm Pl}^2 \dot{H}g^{00} - M_{\rm Pl}^2(3H^2 + \dot{H})\right.$$
$$\left. + \frac{1}{2}M_2^4(g^{00}+1)^2 + \cdots\right],$$
$$(27)$$

where M_2 is a constant mass scale. The action described by eq. (27) demonstrates the incorporation of the Goldstone boson into the metric fluctuations. However, by taking the decoupling limit $M_{\rm Pl} \rightarrow \infty$, $\dot{H} \rightarrow 0$, and keeping $M_{\rm Pl}^2 \dot{H}$ fixed, π can be recovered, and the metric perturbation is expressed in terms of π as $g^{00} + 1 = 2\dot{\pi} - \dot{\pi}^2 + (\partial_i \pi)^2/a^2$. The action then becomes

$$S_\pi = \int dt d^3x a^3 \left[\frac{1}{2}\dot{\pi}_c^2 - \frac{c_s^2}{2}\frac{(\partial_i \pi_c)^2}{a^2}\right.$$
$$\left. + \frac{c_s^{\frac{3}{2}}}{2f_\pi^2}(c_s - 1)^2 \dot{\pi}_c \frac{(\partial_i \pi_c)^2}{a^2} \cdots\right].$$
$$(28)$$

Here, $\pi_c \equiv c_s^{-3/2} f_\pi^2 \pi$ is the canonically normalized Goldstone boson, $f_\pi^4 \equiv 2c_s M_{\rm Pl}^2 |\dot{H}|$ is the symmetry breaking scale, and $c_s^{-2} = 1 - 2M_2^4/M_{\rm Pl}^2|\dot{H}|$ is the reduced sound speed of π_c.

To generate parity-odd signals through the interactions between π and $\vec{A}$, we consider mixing interactions in the form $\sim \pi^2 \vec{A}$, allowing an odd number of spatial derivatives. Up to dimension-7, the interaction action is given by [1]:

$$S_{\pi\sigma} = \int dt d^3x a^3 \left[\rho a^{-2}\partial_i \pi_c A_i - \frac{a^{-2}}{\tilde{\Lambda}}\dot{\pi}_c \partial_i \pi_c A_i\right.$$
$$\left. + \frac{a^{-4}}{\Lambda^3}\partial_j \dot{\pi}_c \partial_i \partial_j \pi_c A_i + \frac{a^{-2}}{\bar{\Lambda}^3}\ddot{\pi}_c \partial_i \dot{\pi}_c A_i\right].$$
$$(29)$$

The couplings are defined as $\rho \equiv 2c_s^{\frac{3}{2}}\omega_1^3/f_\pi^2$, $1/\tilde{\Lambda} \equiv c_s^{\frac{3}{2}}\rho/f_\pi^2$, $1/\Lambda^3 \equiv 2c_s^3\omega_2/f_\pi^4$, and $1/\bar{\Lambda}^3 \equiv 4c_s^3\omega_3/f_\pi^4$, where w_i denote couplings of mass dimensions. Subsequently, the perturbative bounds on these couplings are derived, such that the sizes of these mixing interactions are smaller than both the kinetic terms of the fields π and $\vec{A}$. It is shown in §III.C and Appendix B that the dimension-7 operators $\sim \partial_j \dot{\pi}_c \partial_i \partial_j \pi_c A_i$ and $\sim \ddot{\pi}_c \partial_i \dot{\pi}_c A_i$ lead to sizable signals, while the remaining two dimension-5 operators give negligible parity-odd signals.

F. Dimensional Analysis and Perturbative Criterion

The couplings ρ, $\tilde{\Lambda}$, Λ, and $\bar{\Lambda}$ introduced eq. (29) are free parameters of the theory. To keep them under perturbative control, they are required to be suppressed by some energy scale greater than H. We start by estimating the sizes of the kinetic terms $\sim \dot{\pi}_c^2$ and $\sim \dot{A}^2$. Using eq. (26), the dispersion relations of π and A are

$$\omega = c_s k_p, \quad \omega_A^2 \approx k_p^2 \pm 2\kappa k_p + m_A^2. \quad (30)$$

When differentiating with respect to the proper time t, an additional factor of the angular frequency ω appears. This implies the kinetic terms of the Goldstone boson and the massive spin-1 field scale as $\sim \omega^2 \pi_c$ and $\sim \omega_A^2 A$, respectively. The latter can be rewritten as

$$\sim c_s^{-2}\omega^2 A^2 \gamma(\omega) \quad (31)$$

according to eq. (30), where $\gamma(\omega) \equiv 1 \pm 2\alpha_\kappa(\omega) + \alpha_m^2(\omega)$, $\alpha_\kappa \equiv c_s\kappa/\omega$, and $\alpha_m \equiv c_s m_A/\omega$. Since the low-speed collider regime $c_s \ll m_A/H$ is of our interest, and the parameters are evaluated at the energy scale $\omega = H$, we have $\alpha_\kappa, \alpha_m \ll 1$ and hence $\gamma \sim 1$.

The subluminal sound speed c_s acquired by the Goldstone boson breaks de Sitter boosts [24], resulting in time and space scaling differently. By dimensional analysis, $\int dt d^3x \dot{\pi}_c^2 \sim 1$. Substituting $t \sim 1/\omega$ and $x \sim c_s/\omega$, we obtain:

$$c_s^3\omega^{-4}\dot{\pi}_c^2 \sim 1 \implies \pi_c \sim c_s^{\frac{3}{2}}\omega, \dot{\pi}_c \sim c_s^{\frac{3}{2}}\omega^2. \quad (32)$$

The same reasoning can be applied to A, leading to $A \sim c_s^{-1}\omega\gamma^{-\frac{1}{4}}(\omega)$, and $\dot{A} \sim c_s^{-2}\omega^2\gamma^{-\frac{1}{4}}(\omega)$. The Goldstone boson and massive vector field kinetic terms thus scale as $\sim c_s^{-3}\omega^4$ and $\sim c_s^{-4}\omega^4\gamma^{-\frac{1}{2}}(\omega)$, respectively. As $c_s \ll 1$, the kinetic term of the Goldstone boson is smaller than that of the massive spin-1 field.

By adopting the derived scaling rules above, the mixing interactions scale as[1]

$$\rho\partial_i\pi_c A_i \sim c_s^{-\frac{7}{2}}\rho\omega^3\gamma^{-\frac{1}{4}}(\omega), \quad (33a)$$

$$\frac{1}{\tilde{\Lambda}}\dot{\pi}_c\partial_i\pi_c A_i \sim \frac{1}{\tilde{\Lambda}}c_s^{-5}\gamma^{-\frac{1}{4}}(\omega), \quad (33b)$$

$$\frac{1}{\Lambda^3}\partial_j\dot{\pi}_c\partial_i\partial_j\pi_c A_i \sim \frac{1}{\Lambda^3}c_s^{-7}\omega^7\gamma^{-\frac{1}{4}}(\omega), \quad (33c)$$

$$\frac{1}{\bar{\Lambda}^3}\ddot{\pi}_c\partial_i\dot{\pi}_c A_i \sim \frac{1}{\bar{\Lambda}^3}c_s^{-5}\omega^7\gamma^{-\frac{1}{4}}(\omega). \quad (33d)$$

Demanding the interaction terms in eq. (33a) to (33d) to be less than $c_s^{-3}\omega^4$, the perturbative bounds on the

---

[1] There is a typo in eq. (12) of [1], where the interaction term $\frac{1}{\tilde{\Lambda}}\dot{\pi}_c\partial_i\pi_c A_i$ should scale as c_s^{-5} instead of c_s^{-7}.

couplings are as follows:

$$\frac{\rho}{H} \lesssim c_s^{\frac{1}{2}} \gamma^{\frac{1}{4}}(\omega), \tag{34a}$$

$$\frac{H}{\Lambda} \lesssim c_s^{\frac{4}{3}} \gamma^{\frac{1}{12}}(\omega), \tag{34b}$$

$$\frac{H}{\bar{\Lambda}} \lesssim c_s^{\frac{2}{3}} \gamma^{\frac{1}{12}}(\omega). \tag{34c}$$

In the subsequent section, the physical implications of the interaction between the massive spin-1 field and the Goldstone boson on the trispectrum are analyzed, taking into consideration the constraints given in eq. (34a) to (34c). We begin by providing a brief overview of the EFT approach that enables us to integrate out the massive field A_i from the ultraviolet (UV) complete theory, leading to a non-local single-field theory that remains applicable at low energy.

III. NON-LOCAL EFT

A. Introduction to EFT

The basic idea underlying EFT is to describe the low-energy behaviour of a system by eliminating the effects of high-energy degrees of freedom. Consider a UV Lagrangian $\mathcal{L}_{\mathrm{UV}}(\phi, H)$ that encompasses all information about the system, which ϕ and H denote sets of light and heavy fields, respectively. Given the characteristic energy scale of an experiment, the external states of H are often irrelevant, as they are too heavy to be excited. Therefore, we hope to simplify the problem by constructing an effective theory described by the Lagrangian $\mathcal{L}_{\mathrm{EFT}}(\phi)$, that remains valid at energies well below the mass scale M associated with the heavy fields. The path integral formalism of matching $\mathcal{L}_{\mathrm{EFT}}(\phi)$ to $\mathcal{L}_{\mathrm{UV}}(\phi, H)$ below follows [25 and 26].

All correlators in the UV theory are encoded in the partition function $Z[J]$, which is given by

$$Z_{\mathrm{UV}}[J_\phi, J_H] = \int [D\phi][DH] \exp\left[i \int d^4x \big(\mathcal{L}_{\mathrm{UV}}(\phi, H) + J_\phi \phi + J_H H\big)\right]. \tag{35}$$

Here, the contributions by ϕ and H are expressed separately. The scattering amplitudes can then be extracted from the time-ordered correlation functions using the LSZ reduction formula.

The generating functional of the one-particle irre-

ducible (1PI) diagrams is

$$\Gamma_{\mathrm{UV}}[\phi_b, H_b] = -i \log Z_{\mathrm{UV}}[J_\phi, J_H] - \int d^4x J_\phi(x)\phi_b(x) - \int d^4x J_H(x) H_b(x), \tag{36}$$

where the classical background fields are defined as

$$\phi_b(x) \equiv \frac{\partial \log Z_{\mathrm{UV}}[J_\phi, J_H]}{\partial J_\phi(x)}, H_b(x) \equiv \frac{\partial \log Z_{\mathrm{UV}}[J_\phi, J_H]}{\partial J_H(x)}. \tag{37}$$

Similarly, the EFT theory is defined by the partition function and 1PI generating functional as

$$Z_{\mathrm{EFT}}[J_\phi] = \int [D\phi] \exp\left[i \int d^4x \left(\mathcal{L}_{\mathrm{EFT}}(\phi) + J_\phi(\phi)\right)\right], \tag{38}$$

$$\Gamma_{\mathrm{EFT}}[\phi_b] = -i \log Z_{\mathrm{EFT}}[J_\phi] - \int d^4x J_\phi(x)\phi_b(x), \tag{39}$$

where $\phi_b(x) \equiv \frac{\partial \log Z_{\mathrm{EFT}}(\phi)}{\partial J_\phi(x)}$. To guarantee the UV theory and EFT yield identical physical predictions for light fields, it is necessary to have $\Gamma_{\mathrm{UV}}[\phi, 0] = \Gamma_{\mathrm{EFT}}[\phi]$, where J_H is set to zero in Γ_{UV}.

Expanding eq. (38) and $\mathcal{L}_{\mathrm{EFT}}(\phi)$ around the background field ϕ_b with $\phi = \phi_b + \phi'$, where ϕ_b satisfies $\frac{\partial \mathcal{L}_{\mathrm{EFT}}}{\partial \phi}|_{\phi=\phi_b} = -J_\phi$, we obtain:

$$Z_{\mathrm{EFT}} = \exp\left[i \int d^4x \left(\mathcal{L}_{\mathrm{EFT}}|_{\phi=\phi_b} + J_\phi \phi_b\right)\right] \times \int [D\phi'] \exp\left[-\frac{i}{2} \int d^4x \phi'^T Q_{\mathrm{EFT}} \phi'\right] + \cdots$$
$$= \exp\left[i \int d^4x \left(\mathcal{L}_{\mathrm{EFT}} + J_\phi \phi_b\right)\right] [\det Q_{\mathrm{EFT}}]^{-\frac{1}{2}}, \tag{40}$$

where $Q_{\mathrm{EFT}} \equiv -\frac{\partial^2 \mathcal{L}_{\mathrm{EFT}}}{\partial \phi^2}|_{\phi=\phi_b}$. Substituting eq. (40) into eq. (39) gives

$$\Gamma_{\mathrm{EFT}}[\phi] = \int d^4x \mathcal{L}_{\mathrm{EFT}} + \frac{i}{2} \log \det Q_{\mathrm{EFT}} + \cdots. \tag{41}$$

Repeating the above procedures for the UV theory, the corresponding 1PI generating function is

$$\Gamma_{\mathrm{UV}}[\phi] = \int d^4x \mathcal{L}_{\mathrm{UV}}|_{H=H_b} + \frac{i}{2} \log \det Q_{\mathrm{UV}} + \cdots, \tag{42}$$

where

$$Q_{\mathrm{UV}} \equiv \begin{pmatrix} \Delta_H & X_{LH} \\ X_{LH} & \Delta_L \end{pmatrix} = \begin{pmatrix} -\frac{\partial^2 \mathcal{L}_{\mathrm{UV}}}{\partial H^2} & -\frac{\partial^2 \mathcal{L}_{\mathrm{UV}}}{\partial \phi \partial H} \\ -\frac{\partial^2 \mathcal{L}_{\mathrm{UV}}}{\partial \phi \partial H} & -\frac{\partial^2 \mathcal{L}_{\mathrm{UV}}}{\partial \phi^2} \end{pmatrix}\Bigg|_{H=H_b}. \tag{43}$$

As $J_H = 0$, the background field H_b is determined by the equation $\frac{\partial \mathcal{L}_{\text{UV}}}{\partial H}|_{H=H_b} = 0$, and it becomes a function of ϕ only. By matching eq. (41) and (42), the tree-level effective Lagrangian is identified as

$$\mathcal{L}_{\text{EFT}}^{(0)} = \mathcal{L}_{\text{UV}}(\phi, H_b), \qquad (44)$$

where $\frac{\partial \mathcal{L}_{\text{UV}}}{\partial H}|_{H=H_b} = 0$. In other words, the tree-level effective action $S_{\text{EFT}}^{(0)}$ can be obtained with ease by first solving $\frac{\partial \mathcal{L}_{\text{UV}}}{\partial H}|_{H=H_b} = 0$, and substituting the solution H_b into S_{UV}.

In general, $\mathcal{L}_{\text{EFT}}(\phi)$ is non-local, meaning it contains non-polynomial terms in the fields and their derivatives, such as $\mathcal{L}_{\text{EFT}}(\phi) \supset \phi(\Box + M^2)^{-1}\phi$. Yet, if H are much heavier than the light fields, the exchange of H between ϕ can be treated as a local interaction involving ϕ only, where $(\Box + M^2)^{-1}$ can be locally expanded as $\sim M^{-2} - M^{-4}\Box + \cdots$. In the following, we investigate how a non-local EFT description emerges from the interaction action between π and $\vec{A}$.

B. Effective Action

Combining eq. (25), (28), and (29), the action of the UV theory is

$$S_{\text{UV}} = \int dt d^3 x a^3 \left[\frac{1}{2}\dot{\pi}_c^2 - \frac{c_s^2}{2}\frac{(\partial_i \pi_c)^2}{a^2} \right.$$
$$\left. - \frac{1}{2a^2} A_i \left[\delta_{ij}(\partial_t^2 + H\partial_t) + \mathcal{D}_{ij} \right] A_j + \frac{A_i}{a^2} J_i(\pi_c) \right]. \qquad (45)$$

Here, $\mathcal{D}_{ij}$ represents the spatial part of the kinetic operator of the massive spin-1 field:

$$\mathcal{D}_{ij} \equiv \left(-\frac{\partial_i^2}{a^2} + m_A^2 \right)\delta_{ij} - 2\kappa\varepsilon_{ijl}\frac{\partial_l}{a}, \qquad (46)$$

and the current term is

$$J_i(\pi_c) \equiv -\frac{1}{\tilde{\Lambda}}\dot{\pi}_c \partial_i \pi_c + \frac{a^{-2}}{\Lambda^3}\partial_j \pi_c \partial_i \partial_j \pi_c + \frac{1}{\Lambda^3}\ddot{\pi}_c \partial_i \dot{\pi}_c. \qquad (47)$$

Using the approach outlined in §III.A, the massive field A_i can be integrated out to obtain the tree-level effective action, which is[2]

$$S_{\text{EFT}} = \int dt d^3 x a^3 \left[\frac{1}{2}\dot{\pi}_c^2 - \frac{c_s^2}{2}\frac{(\partial_i \pi_c)^2}{a^2} \right.$$
$$\left. + \frac{1}{2a^2} J_i(\pi_c) \left[(\partial_t^2 + H\partial_t) + \mathcal{D} \right]_{ij}^{-1} J_j(\pi_c) \right], \qquad (48)$$

———

[2] The (0) superscript on $S_{\text{EFT}}^{(0)}$ has been dropped for convenience.

One can expand the inverse operator in eq. (48) into an infinite sum, resulting in the following expression:

$$S_{\text{EFT}} = \int dt d^3 x a^3 \left[\frac{1}{2}\dot{\pi}_c^2 - \frac{c_s^2}{2}\frac{(\partial_i \pi_c)^2}{a^2} \right.$$
$$\left. + \frac{1}{2a^2} J_i(\pi_c)\mathcal{D}_{ij}^{-1} J_j(\pi_c) + \mathcal{O}(\partial_t^2) \right]. \qquad (49)$$

The presence of inverse spatial derivatives in $\mathcal{D}_{ij}^{-1}$ indicates the spatial non-locality of the action. It can be further decomposed into parity-odd and parity-even components as $\mathcal{D}_{ij}^{-1} = [\mathcal{D}_{\text{PO}}^{-1}]_{ij} + [\mathcal{D}_{\text{PE}}^{-1}]_{ij}$, where

$$[\mathcal{D}_{\text{PO}}^{-1}]_{ij} \equiv \frac{2\kappa\varepsilon_{ijl}\partial_l/a}{(-\partial_i^2/a^2 + m_A^2)^2 + 4\kappa^2\partial_i^2/a^2}, \qquad (50)$$

$$[\mathcal{D}_{\text{PE}}^{-1}]_{ij} \equiv \frac{(-\partial_i^2/a^2 + m_A^2)\left[\delta_{ij} + \frac{4\kappa^2\partial_i\partial_j/a^2}{(-\partial_i^2/a^2 + m_A^2)^2}\right]}{(-\partial_i^2/a^2 + m_A^2)^2 + 4\kappa^2\partial_i^2/a^2}. \qquad (51)$$

According to the UV theory, the appearance of parity-odd signals can be traced back to the inclusion of an extra massive spin-1 field, which evades the no-go theorem by violating the single-field requirement. On the contrary, the EFT approach attributes parity violation to the presence of the ε_{ijl} factor in the denominator of $[\mathcal{D}_{\text{PO}}^{-1}]_{ij}$, as depicted in eq. (50). Moving forward, the magnitude of parity-odd signals in the trispectrum τ is estimated.

C. Estimating Size of Parity-Odd Signals

A simple estimation of the parity-odd trispectrum is given by $\sim \frac{\mathcal{L}_{4,\text{PO}}}{\mathcal{L}_2}\Delta_\zeta^{-2}$, where Δ_ζ refers to the dimensionless power spectrum, and the quadratic Lagrangian $\mathcal{L}_2$ is taken to be the Goldstone kinetic term $\sim c_s^{-3}\omega^4$. Evaluating $\mathcal{D}_{\text{PO}}^{-1}$ at the Hubble scale $\omega \sim H$, we get

$$\mathcal{D}_{\text{PO}}^{-1} \sim \left(\frac{c_s}{H}\right)^2 \frac{\alpha_\kappa}{(1 + \alpha_m^2)^2 + 4\alpha_\kappa^2}, \qquad (52)$$

where $\partial_i/a \sim H/c_s$ is substituted.

There are two dimension-7 operators in the effective action: $\sim \partial_j\dot{\pi}_c\partial_i\partial_j\pi_c A_i$ and $\sim \ddot{\pi}_c\partial_i\dot{\pi}_c A_i$. Without loss of generality, we focus on the former (refer to Appendix B for the latter), which results in the following quartic parity-odd Lagrangian:

$$\mathcal{L}_{4,\text{PO}} \sim \frac{1}{\Lambda^6}\partial_l\dot{\pi}_c\partial_i\partial_l\pi_c[\mathcal{D}_{\text{PO}}^{-1}]_{ij}\partial_k\dot{\pi}_c\partial_j\partial_k\pi_c. \qquad (53)$$

Substituting $\partial_i/a \sim H/c_s$, $\dot{\pi}_c \sim c_s^{-\frac{3}{2}}H^2$, $\pi_c \sim c_s^{-\frac{3}{2}}H$, and using eq. (52), eq. (53) becomes

$$\mathcal{L}_{4,\text{PO}} \sim \frac{1}{\Lambda^6}c_s^{-10}H^{10}\frac{\alpha_\kappa}{(1 + \alpha_m^2)^2 + 4\alpha_\kappa^2}. \qquad (54)$$

The contribution to the parity-odd trispectrum is there-

fore

$$\tau_{\text{PO}}^{\partial_j \dot{\pi}_c \partial_i \partial_j \pi_c A_i} \sim \frac{\mathcal{L}_{4,\text{PO}}}{c_s^{-3} H^4} \Delta_\zeta^{-2}$$

$$= c_s^{-7} \left(\frac{H}{\Lambda} \right)^6 \frac{\alpha_\kappa \Delta_\zeta^{-2}}{(1 + \alpha_m^2)^2 + 4\alpha_\kappa^2}. \qquad (55)$$

Finally, using the perturbativity bound stated in eq. (34b) gives

$$\tau_{\text{PO}}^{\partial_j \dot{\pi}_c \partial_i \partial_j \pi_c A_i} \sim c_s \alpha_\kappa \Delta_\zeta^{-2} = \mathcal{O}(10^6), \qquad (56)$$

which $c_s = 0.1$ is used and the factor $\gamma \sim 1$ is dropped. In comparison with the parity-even trispectrum $\tau_{\text{PE}} \lesssim 2800$ [27], the estimation by eq. (56) seems to be too large. Upon applying the Schwinger-Keldysh formalism [28], as discussed in the next section, the actual size of the trispectrum is found to be further suppressed by c_s^4, leading to $\tau_{\text{PO}}^{\partial_j \dot{\pi} c \partial i \partial_j \pi_c A_i} \sim \mathcal{O}(10^2)$. A similar analysis has been conducted to derive $\tau_{\text{PO}}^{\dot{\pi}_c \partial i \pi_c A_i} \sim c_s \alpha_\kappa$ [1], which yields minor parity-odd contributions for $\alpha_\kappa \ll 1$.

D. Trispectrum and its Shape Characteristics

In [1], the Schwinger-Keldysh formalism is applied to calculate the s-channel contribution to the parity-odd trispectrum. The result is

$$\langle \pi_c^4 \rangle'_{s,\text{PO}} = -\frac{1}{\Lambda^6} \vec{s} \cdot (\vec{k}_1 \times \vec{k}_3)(\vec{k}_1 \cdot \vec{k}_2)(\vec{k}_3 \cdot \vec{k}_4)$$

$$\times 2i \, \text{Im} \left\{ 2\pi i \text{Res}_{\tau \to \tau_c} \left(a^{-1} \mathcal{K}_1^+ \overset{\leftrightarrow}{\partial}_\tau \mathcal{K}_2^+ \right) \right.$$

$$\left[\frac{2\kappa a}{(s^2 + m_A^2 a^2)^2 - 4\kappa^2 a^2 s^2} + \mathcal{O}(\partial_\tau^2) \right]$$

$$\left. \left(a^{-1} \mathcal{K}_3^+ \overset{\leftrightarrow}{\partial}_\tau \mathcal{K}_4^+ \right) \right\}. \qquad (57)$$

Here, $\vec{s} \equiv \vec{k}_1 + \vec{k}_2$ is the exchanged momentum of the s-channel, τ_c is a singularity point defined as

$$\tau_c \equiv \frac{1}{s} \left(-\frac{\kappa}{H} + \frac{im_A}{H} \sqrt{1 - \frac{\kappa^2}{m_A^2}} \right), \qquad (58)$$

$\mathcal{K}_i^+$ is the bulk-to-boundary propagator of the Goldstone boson given by

$$\mathcal{K}_i^+ \equiv \frac{H^2}{2c_s^3 k_i^3} (1 - ic_s k_i \tau) e^{ic_s \tau}, \qquad (59)$$

and $f \overset{\leftrightarrow}{\partial}_\tau g \equiv f \partial_\tau g - g \partial_\tau f$. Relating the curvature perturbation to the Goldstone boson by $\zeta = -H\pi + \mathcal{O}(\pi^2) \approx$

$-Hc_s^{-\frac{3}{2}} f_\pi^{-2} \pi_c$ [24], the dimensionless trispectrum $\mathcal{T}$ is

$$\langle \zeta_{\vec{k}_1} \zeta_{\vec{k}_2} \zeta_{\vec{k}_3} \zeta_{\vec{k}_4} \rangle' = \pi^6 \Delta_\zeta^6 \frac{k_T^3}{(\Pi_{i=1}^4 k_i)^3} \mathcal{T}(\vec{k}_1, \vec{k}_2, \vec{k}_3, \vec{k}_4), \quad (60)$$

where $k_T = \sum_{i=1}^4 k_i$ is the total energy. At LO, the parity-odd component of $\mathcal{T}$ is

$$\mathcal{T}_{\text{PO}}(\vec{k}_1, \vec{k}_2, \vec{k}_3, \vec{k}_4) = \mathcal{A}_{\text{PO}} \Pi_s(\{\vec{k}_i\}) F_s(\{k_i\}, s) + (t, u). \qquad (61)$$

In eq. (61), $\mathcal{A}_{\text{PO}}$ and Π_s represent the amplitude and polarization factor of $\mathcal{T}$, respectively, and have the following expressions:

$$\mathcal{A}_{\text{PO}} \equiv \frac{i}{(2\pi)^2 c_s^2 \Delta_\zeta^2} \left(\frac{H}{\Lambda} \right)^4 \left(\frac{\kappa}{H} \right) \left(\frac{m_A}{2H} \right)^4, \qquad (62)$$

$$\Pi_s(\{\vec{k}_i\}) \equiv \vec{s} \cdot (\vec{k}_1 \times \vec{k}_3)(\vec{k}_1 \cdot \vec{k}_2)(\vec{k}_3 \cdot \vec{k}_4). \qquad (63)$$

The function $F_s(\{k_i\}, s)$ is defined as

$$F_s(\{k_i\}, s) \equiv \frac{64(k_1 - k_2)(k_3 - k_4)}{k_T^3 s^2} \, \text{Im} \left[e^{ic_s k_T \tau_c} \right.$$

$$\left. \times \frac{i\pi(H\tau_c)^6 (ik_{12} + c_s k_1 k_2 \tau_c)(ik_{34} + c_s k_3 k_4 \tau_c)}{m_A^4 \kappa(\kappa + sH\tau_c)}, \right. \tag{64}$$

where $k_{ij} \equiv k_i + k_j$.

As mentioned in §III.C, there is an additional c_s^4 suppression to the actual size of the trispectrum. Indeed, by substituting $\alpha_\kappa \equiv c_s \kappa/\omega$ into eq. (62), $\mathcal{A}_{\text{PO}} \sim c_s^{-3} \Delta_\zeta^{-2}$ is obtained. We also notice the factor Π_s given by eq. (63) vanishes if all $\vec{k}_i$ are coplanar.

The parity-odd dimensionless trispectrum, as demonstrated in eq. (61), exhibits intriguing features in its shape. Applying eq. (58), the exponential factor in $F_s(\{k_i\}, s)$ can be broken down into its real and imaginary parts:

$$e^{ic_s k_T \tau_c} = \exp \left(-\frac{k_T}{s} \sqrt{\alpha_m^2 - \alpha_\kappa^2} \right) \exp \left(-\frac{i\alpha_\kappa k_T}{s} \right). \tag{65}$$

The real part of eq. (65) implies the magnitude of the parity-odd signals scales as $\sim e^{-c_s m_A/H}$, which can be quite large, as our focus is on the low-speed regime where $c_s \ll m_A/H$. The magnitude of the trispectrum can be estimated as

$$|\mathcal{T}_{s,\text{PO}}| \sim \left(\frac{k_S}{k_L} \right)^n \exp \left(-\sqrt{\alpha_m^2 - \alpha_\kappa^2} \times \frac{4k_S}{k_L} \right), \qquad (66)$$

where $k_S \sim k_i$ are the short modes and $k_L \sim s$ is the long mode. By differentiating eq. (66) with respect to k_S/k_L and setting the derivative to 0, the resonance peak

is found to locate at:

$$\frac{k_S}{k_L} \sim \frac{4}{n}\sqrt{\alpha_m^2 - \alpha_\kappa^2}. \qquad (67)$$

Without the chemical potential, eq. (67) reduces to $k_S/k_L \sim \alpha_m = c_s m_A/H$, which represents the same resonance peak as the usual low-speed collider regime [24]. Meanwhile, the imaginary part of eq. (65) suggests the trispectrum demonstrates oscillatory behaviour with respect to the ratio k_S/k_L, where the angular frequency $\alpha_\kappa \equiv c_s \kappa/H$ is determined by the reduced sound speed of the Goldstone boson and the chemical potential, and independent of the vector boson mass.

Throughout §II and §III, the theoretical foundations of the parity-odd contributions to the trispectrum have been studied. The upcoming sections continue to focus on the practical implementation of measuring the parity-odd 4PCF using our developed codes. We commence with an illustration using a toy model of tetrahedra.

IV. TOY MODEL OF TETRAHEDRA

In line with the approach in [3], a toy model consisting of 1500 tetrahedra within a cubic box with a side length of $L = 1000$ has been constructed. The purpose of this toy model is to assess the functionality of our 4PCF estimator codes. Each tetrahedron in the model has three sides extending from the primary vertex, with lengths $r_1 \sim 10$, $r_2 \sim 20$, and $r_3 \sim 30$. In order to enhance the realism of each tetrahedron, a random rotation is introduced to every vertex, where the rotation angle θ is selected from the range of $[-180°, 180°]$ for each of the three Cartesian coordinates. Additionally, random distances $\Delta r_1 \in [0, 1]$, $\Delta r_2 \in [-2, 2]$, and $\Delta r_3 \in [-1, 0]$ are incorporated to modify the values of r_1, r_2, and r_3 respectively. To achieve minimal overlap between tetrahedra, a minimum separation of 60 (roughly twice the longest side r_3 of the tetrahedron) between any two primary vertices is imposed.

For a given tetrahedron, we select one point as the origin and assign subscripts to three vectors originating from it, ensuring $r_1 < r_2 < r_3$. To determine the handedness, we observe the directions when looking down from the origin along each vector $\vec{r}_i$. The direction from $\vec{r}_1$ to $\vec{r}_3$ defines the handedness, as illustrated in FIG. 3 [2]. FIG. 4 shows an example cubic box filled with 1500 counterclockwise tetrahedra.

To verify the functionality of our codes, we proceed to calculate the 4PCF estimator for each tetrahedron, considering both counterclockwise and clockwise tetrahedra. The computation is performed within a specific radial range: $r_1 \in [5, 15]$, $r_2 \in [15, 25]$, and $r_3 \in [25, 35]$. This restriction guarantees only the vertex with three sides of lengths $r_1 \sim 10$, $r_2 \sim 20$, and $r_3 \sim 30$ is considered as the primary vertex. The purpose of this selection is to illustrate the connection between the handedness of a tetrahedron and the parity-odd 4PCF. The obtained
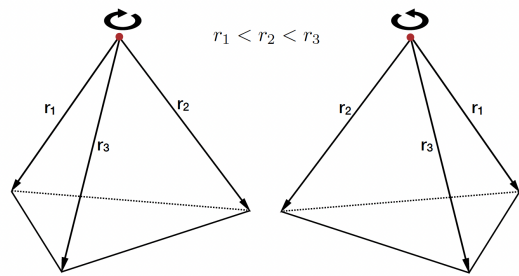

FIG. 3: We define the handedness of a tetrahedron by the direction of $\vec{r}_1$ to $\vec{r}_3$ when viewed from the origin. [2]
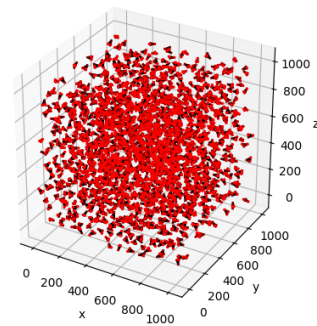

FIG. 4: A cubic box with a side length of $L = 1000$ is depicted, and it contains 1500 counterclockwise tetrahedra. Each tetrahedron has a primary vertex, from which three sides extend with lengths $r_1 \sim 10$, $r_2 \sim 20$, and $r_3 \sim 30$.

results are presented in FIG. 5 and 6, using angular momentum multipoles $(1, 1, 1)$ and $(1, 2, 2)$, respectively.
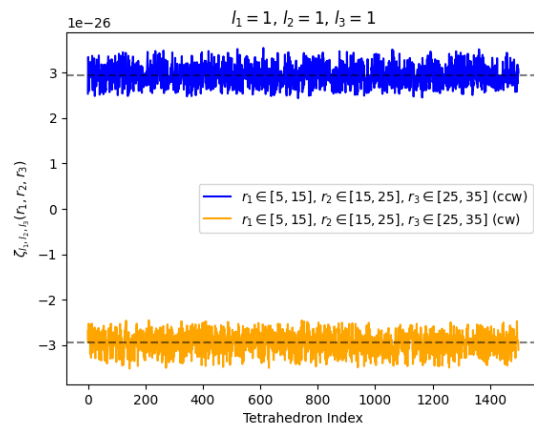

FIG. 5: 4PCF estimators of 1500 counterclockwise (ccw) and clockwise (cw) tetrahedra, using angular momentum multipole $(1, 1, 1)$. The dotted line represents the mean value of the 1500 tetrahedra. Clockwise tetrahedra yield the exact same value as their counterclockwise counterparts, but with the opposite sign.
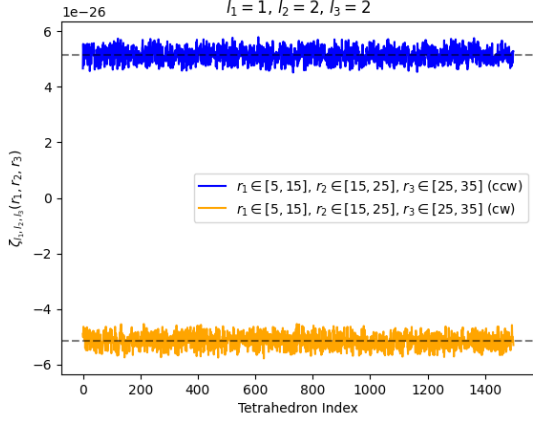
FIG. 6: 4PCF estimators of 1500 counterclockwise (ccw) and clockwise (cw) tetrahedra, using angular momentum multipole $(1, 2, 2)$. The dotted line represents the mean value of the 1500 tetrahedra. Clockwise tetrahedra yield the exact same value as their counterclockwise counterparts, but with the opposite sign.

The lowest-lying parity-odd isotropic basis function corresponds to the subscripts $l_1 = l_2 = l_3 = 1$. Putting this into eq. (8),

$$\mathcal{P}_{111}(\hat{\vec{r}}_1, \hat{\vec{r}}_2, \hat{\vec{r}}_3) = -\frac{3i}{\sqrt{2}(4\pi)^{\frac{3}{2}}}\hat{\vec{r}}_1 \cdot (\hat{\vec{r}}_2 \times \hat{\vec{r}}_3). \qquad (68)$$

As anticipated, the counterclockwise tetrahedra give a positive projection on this function, while the clockwise tetrahedra gives a negative projection (see FIG. 5).

In a given tetrahedron, any of its four vertices can be chosen as the primary vertex. Among these vertices, some are considered "counterclockwise" while others are deemed "clockwise." When the 4PCF estimators are placed in the same radial bin and angular momentum multipole (l_1, l_2, l_3), there is a possibility of internal cancellation occurring between positive and negative values, which diminishes parity-odd signals. To reduce the internal cancellation, it is preferable to use finer binning. The effect of using finer binning is demonstrated in §V.

V. DATA

Our test sample consists of 1000 galaxies extracted from the twelfth data release (DR12) [29] of the SDSS-III [11] as part of the BOSS. Two samples, namely CMASS and LOWZ, are included in the survey, and we use the former for our study. Luminous Red Galaxies (LRGs) account for approximately 74% in the CMASS sample, while the rest are late-type spirals [30]. To analyze the data, we divide the radial range $r_i \in [20, 160]h^{-1}$Mpc into 10 evenly spaced bins, with a width of $\Delta r = 14h^{-1}$Mpc. Furthermore, we impose the conditions $r_2 > r_1 + \Delta r$ and $r_3 > r_2 + \Delta r_1$, resulting in a total of 56

radial bins. The impact of finer binning is also investigated by employing 18 evenly spaced bins covering a range of $r_i \in [20, 164]h^{-1}$Mpc, giving a total of 816 radial bins. Due to time constraints, we only expand the parity-odd 4PCF in angular momentum multipoles $(1, 1, 1)$ and $(1, 2, 2)$. Our codes have not yet incorporated edge-correction.

To convert angles and redshifts to Cartesian coordinates, a fiducial cosmology with parameters $\Omega_m = 0.31$, $\Omega_\Lambda = 0$, $\Omega_r h^2 = 4.165 \times 10^{-5}$, $\Omega_k = 1 - (\Omega_m + \Omega_r + \Omega_\Lambda)$, and $h = 0.676$ is employed. In practice, the integral presented in eq. (13) needs to be transformed into a sum over discrete galaxies, where each galaxy is assigned a weight based on

$$w = w_{\text{fkp}}w_{\text{sys}}(w_{\text{noz}} + w_{\text{cp}} - 1), \qquad (69)$$

which w_{fkp} represents the FKP weight [31], w_{sys} is the systematic weight that combines stellar density and seeing, w_{noz} accounts for the redshift failure weight, and w_{cp} represents the fibre collision weight. The redshift failure weight w_{noz} is a factor corresponding to galaxies in the sample whose redshift measurements were unsuccessful or unreliable. This factor is used to downweight or exclude such galaxies from the analysis to prevent their influence on the results. On the other hand, the fibre collision weight w_{cp} is applied to account for pairs of galaxies which have overlapping fibre collision zones in the spectroscopic observations. These collisions occur when two galaxies are so close such that only one of them can be assigned a spectrum because of the limited fibre size. The fibre collision weight adjusts the weights of these galaxies to eliminate the effects of incomplete sampling caused by the collisions. Eq. (13) is then rewritten as

$$\hat{\zeta}_{l_1 l_2 l_3}(r_1, r_2, r_3) = \sum_{i=1}^{N_g} \sum_{m_1 m_2 m_3} \begin{pmatrix} l_1 & l_2 & l_3 \\ m_1 & m_2 & m_3 \end{pmatrix} \qquad (70)$$
$$\times w_i a_{l_1 m_1}(\vec{x}_i; r_1) a_{l_2 m_2}(\vec{x}_i; r_2) a_{l_3 m_3}(\vec{x}_i; r_3).$$

The computed 4PCF estimators are displayed in FIG. 7, 8, 9, and 10. FIG. 7 and 8 demonstrate the results using angular momentum multipoles $(1, 1, 1)$ and $(1, 2, 2)$ respectively, with $\Delta r = 14h^{-1}$Mpc being the bin width. Their sizes are comparable, both with an order of $\sim 10^{-17}$. FIG. 9 shows $\hat{\zeta}_{111}$ with a finer binning of $\Delta r = 8h^{-1}$Mpc, which gives an order of roughly 10^2 bigger than the measurement using $\Delta r = 14h^{-1}$Mpc, which is consistent with our expectation. For visibility, we rescale the 4PCF in FIG. 9 by multiplying a factor of $r_1 r_2 r_3$, and the result is illustrated in FIG. 10.
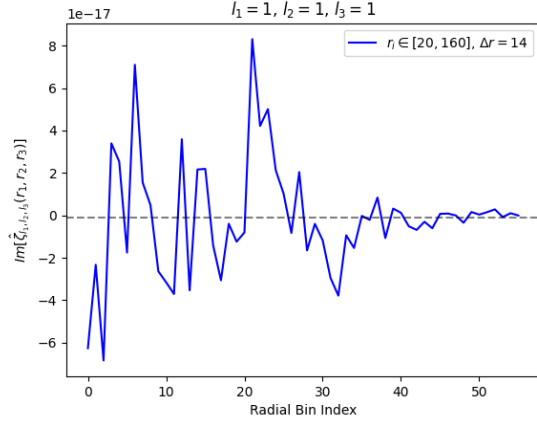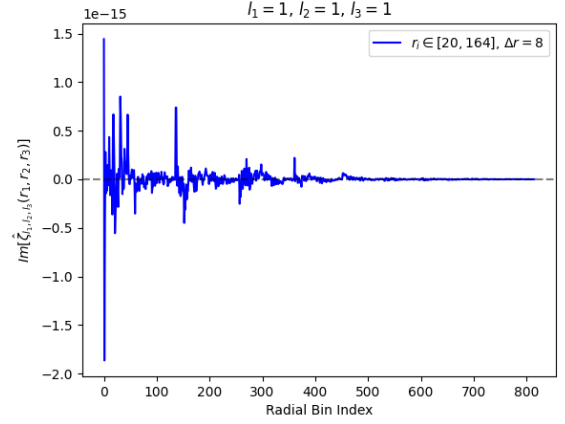
FIG. 7: Measurement of $\hat{\zeta}_{111}$ from the test sample. The measurement was performed using 10 evenly spaced bins covering a range of $r_i \in [20, 160]h^{-1}\mathrm{Mpc}$. The dotted line represents the mean value across all radial bins.
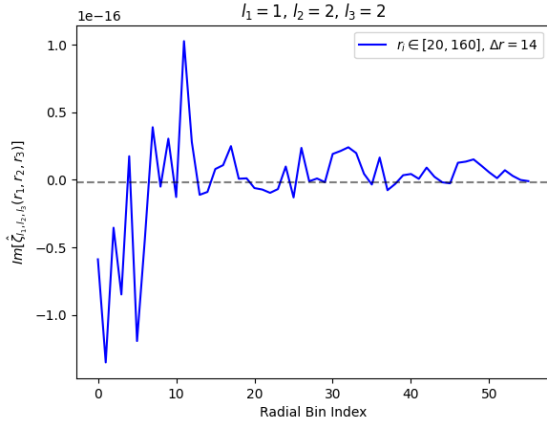

FIG. 9: Measurement of $\hat{\zeta}_{111}$ from the test sample. The measurement was performed using 18 evenly spaced bins covering a range of $r_i \in [20, 164]h^{-1}\mathrm{Mpc}$. The dotted line represents the mean value across all radial bins.

FIG. 8: Measurement of $\hat{\zeta}_{122}$ from the test sample. The measurement was performed using 10 evenly spaced bins covering a range of $r_i \in [20, 160]h^{-1}\mathrm{Mpc}$. The dotted line represents the mean value across all radial bins.
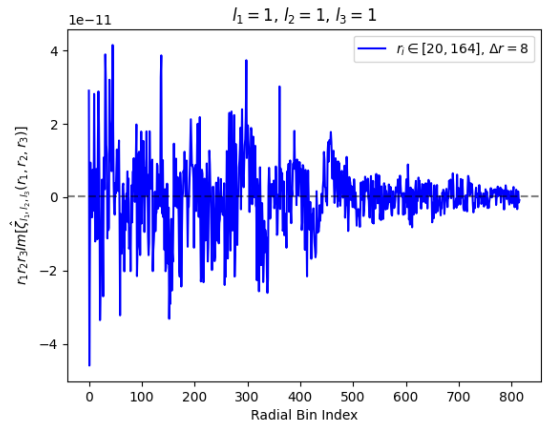

FIG. 10: Same as FIG. 9, but rescaled by a factor of $r_1 r_2 r_3$.

VI. OUTLOOK

A. Coding Limitations

To assess the statistical significance of the parity-odd signals in the 4PCF, it is necessary to compare the signals observed in the BOSS data with those obtained from mock catalogs. This approach follows the methodology described in [**2**] and [**3**], which involves conducting a non-parametric rank test.

In the non-parametric rank test, the null hypothesis of zero parity-odd 4PCF is examined, and the test statistic is calculated as follows:

$$\tilde{\chi}^2 = \zeta^T \tilde{C}^{-1} \zeta. \tag{71}$$

Here, ζ represents a vector of the measured parity-odd 4PCF estimators, and $\tilde{C}$ is the theoretical covariance matrix. To conduct the test, $\tilde{\chi}^2$ is computed for both the BOSS data and each of the mock catalogs. The confidence level is upper-constrained at $(1 - 1/N_{\mathrm{mocks}})$, where N_{mocks} refers to the total number of mock catalogs available.

Before proceeding with the non-parametric rank test, a challenge has been identified in the research progress thus far. The computational time required for calculating the parity-odd 4PCF remains substantial, even with a reduced complexity of $\mathcal{O}(N_g^2)$ compared to the original $\mathcal{O}(N_g^4)$. TABLE I provides a summary of the estimated computation time required for calculating parity-odd 4PCF estimators on our local computer, which uses Apple M1 as the central processing unit (CPU).

In the calculations of the parity-odd 4PCF, the summation in eq. (70) involves counting pairs of galaxies,

TABLE I: Estimated computation time of parity-odd 4PCF estimators. N_r denotes the number of radial bins, and $t_{l_1 l_2 l_3 N_r}$ represents the amount of time in unit of hours.

N_r	(l_1, l_2, l_3)	$t_{l_1 l_2 l_3 N_r}$ (hr)
56	$(1,1,1)$	~ 0.5
56	$(1,2,2)$	~ 1.5
816	$(1,1,1)$	~ 9

leading to an expected computation time that scales as N_g^2. In addition, the complexity increases linearly with the number of radial bins N_r. Given the tremendous computation time required, as exemplified in TABLE I, conducting a non-parametric rank test to extract the statistical significance of the parity-odd signals from the BOSS dataset is currently infeasible. To resolve this issue, we are developing codes that utilize GPU acceleration to reduce the computation time.

B. Systematic Uncertainties

Apart from validating the results reported by [2 and 3] with programming, any systematic uncertainties should be carefully addressed. In particular, simulations in the mock catalogs may underestimate the data's covariance, misinterpreting the noise fluctuations as signals [32].

In [32], the BOSS CMASS and LOWZ datasets were reanalyzed using an upgraded suite of BOSS mocks called GLAM-Uchuu galaxy catalogs [33]. These catalogs incorporate full N-body simulations that accurately capture the evolution of 8×10^9 dark matter particles, taking nonlinear gravitational evolution and the redshift-dependent evolution of galaxy clustering into account. In contrast, the formerly used MultiDark-Patchy suite [34] is an approximate model of gravitational evolution, which does not contain full N-body simulations. Following the reanalysis, the statistical significance reported in [2] is drastically reduced from $> 3.5\sigma$ to 1.4σ, indicating the previous results may have been affected by significant systematic uncertainties.

Another potential systematic error to consider is the sub-leading relativistic corrections of the redshift-space distortions (RSD), which may induce false signals of parity violation in the observed trispectrum on large scales [35].

VII. CONCLUSION

This paper studies the potential cosmological parity violation arising from the coupling between a massive spin-1 field and a Goldstone boson, which results from broken time-translations invariance during inflation. By introducing an additional massive field, it becomes possible to circumvent the no-go theorem and induce parity-odd signals on the trispectrum. The effective action, derived using the EFT approach, leads to the emergence of spatial non-locality. Through dimensional analysis, the interaction terms are enforced to remain within perturbative constraints, while demonstrating that the dimension-7 operators generate considerably large signals. A more detailed analysis using the Schwinger-Keldysh formalism reveals an extra c_s^4 suppression on the signals. Without loss of generality, our analysis focuses on the s-channel contribution to the parity-odd trispectrum, which exhibits a resonance peak similar to the original low-speed collider regime. The parity-odd trispectrum's magnitude scales as $\sim e^{-c_s m_A/H}$, and it oscillates with respect to the ratio k_S/k_L, with a frequency dependent on both the reduced sound speed of the Goldstone boson and the chemical potential associated with the inflaton field.

To facilitate the search for evidence of parity violation, the code for computing the 4PCF estimator of the BOSS galaxy example has been successfully established in this work. The functionality of the code has been demonstrated using a toy model of 1500 tetrahedra. $\hat{\zeta}_{111}$ and $\hat{\zeta}_{122}$ of the 4PCF estimator have been computed using 1000 galaxies from the BOSS CMASS galaxy sample. Two different sets of radial bins are employed, with a binning width of $\Delta r = 8h^{-1}$Mpc and $\Delta r = 14h^{-1}$Mpc, respectively. For the former, the 4PCF components corresponding to angular momentum multipoles $(1,1,1)$ and $(1,2,2)$ are computed, both giving a comparable size of $\sim 10^{-17}$. For multipole $(1,1,1)$, we have also applied a finer binning of $\Delta r = 8h^{-1}$Mpc, yielding a result roughly 10^2 times larger than with $\Delta r = 14h^{-1}$Mpc. On account of the substantial computation time required, conducting a non-parametric rank test to extract the statistical significance is currently impractical. To address this issue, GPU-accelerated computation will be utilized to speed up the calculations.

With the abundance of spectroscopic data expected over the next decade from surveys like DESI [36], Euclid [37], and the Rubin Observatory [38], galaxy surveys seem to be ideal for hunting for evidence of parity-violating interactions. These large-scale surveys could help confirm whether the previously observed parity-odd 4PCF actually exist in our universe.

Appendix A: Equation of Motion of Massive Spin-1 Field

We use the conformally flat metric provided in eq. (18). Starting from eq. (19), the Lagrangian of the massive spin-1 field is identified as

$$\mathcal{L} = \sqrt{-g}\left[-\frac{1}{4}F_{\mu\nu}F^{\mu\nu} + \frac{1}{2}m_A^2 A_\mu A^\mu - \frac{1}{4\Lambda_\kappa}\phi F_{\mu\nu}\tilde{F}^{\mu\nu} \right]. \tag{A1}$$

The equation of motion for the vector field can be derived by substituting eq. (A1) into the Euler-Lagrange

equation:

$$\frac{\partial \mathcal{L}}{\partial A_\nu} - \partial_\mu \left(\frac{\partial \mathcal{L}}{\partial(\partial_\mu A_\nu)} \right) = 0. \tag{A2}$$

The partial derivatives are calculated to be

$$\begin{cases} \frac{\partial \mathcal{L}}{\partial A_\nu} = \sqrt{-g}\, m_A^2 A^\nu, \\ \frac{\partial \mathcal{L}}{\partial(\partial_\mu A_\nu)} = \sqrt{-g}\, F^{\mu\nu} + \frac{1}{2\Lambda_\kappa}\phi \varepsilon^{\mu\nu\rho\sigma} F_{\rho\sigma}. \end{cases} \tag{A3}$$

Putting eq. (A3) into eq. (A2) leads to

$$\sqrt{-g}\, m_A^2 A^\nu - \partial_\mu(\sqrt{-g}\, F^{\mu\nu})$$
$$- \frac{1}{2\Lambda_\kappa}\left[\phi\partial_\mu(\varepsilon^{\mu\nu\rho\sigma} F_{\rho\sigma}) + (\partial_\mu\phi)\varepsilon^{\mu\nu\rho\sigma} F_{\rho\sigma}\right] = 0. \tag{A4}$$

To simplify eq. (A4), we should supplement it with the Bianchi identity $\partial_\mu(\varepsilon^{\mu\nu\rho\sigma} F_{\rho\sigma}) = 0$. Furthermore, we notice the inflaton field ϕ depends only on time, i.e. $\partial_i \phi = 0$, where $i = 1, 2, 3$ represent the spatial coordinates. eq. (A4) is hence transformed into

$$\sqrt{-g}\, m_A^2 A^\nu - \partial_\mu(\sqrt{-g}\, F^{\mu\nu}) - \frac{\phi_0'}{2\Lambda\kappa}(\varepsilon^{0\nu\rho\sigma} F_{\rho\sigma}) = 0. \tag{A5}$$

To calculate $\partial_\mu(\sqrt{-g}\, F^{\mu\nu})$, we choose the Coulomb gauge $A_0 = \partial_\mu(\sqrt{-g}\, A^\mu) = 0$ and obtain:

$$\partial_\mu(\sqrt{-g}\, F^{\mu\nu}) = \partial_\mu(\sqrt{-g}(\partial^\mu A^\nu - \partial^\nu A^\mu))$$
$$= \sqrt{-g}\,\partial_\mu\partial^\mu A^\nu$$
$$= a^2(-\partial_\tau^2 + \partial_i^2) A^\nu. \tag{A6}$$

The last term on the left hand side of eq. (A5) can be simplified by computing

$$\varepsilon^{0\nu\rho\sigma} F_{\rho\sigma} = \varepsilon^{0\nu\rho\sigma}(\partial_\rho A_\sigma - \partial_\sigma A_\rho)$$
$$= 2(\nabla \times \vec{A})_\nu, \tag{A7}$$

in which the identity $(\nabla \times \vec{A})_i \equiv \varepsilon_{ijk}\partial_j A_k$ is applied. Finally, by substituting eq. (A6) and (A7) back into eq. (A5), and using the relation $A^\nu = a^{-2} A_\nu$ for spatial components ν, we arrive at the following expression:

$$A_\nu'' - \partial_i^2 A_\nu - \frac{a\dot{\phi}_0}{\Lambda_\kappa}(\nabla \times \vec{A})_\nu + a^2 m_A^2 A_\nu = 0. \tag{A8}$$

eq. (A8) is equivalent to eq. (14) when we switch to vector form:

$$\vec{A}'' - \nabla^2\vec{A} - \frac{a\dot{\phi}_0}{\Lambda_\kappa}\nabla \times \vec{A} + a^2 m_A^2 \vec{A} = 0 \quad \blacksquare$$

Appendix B: Estimating Size of Parity-Odd Signal from a Dimension-7 Operator

In this section, the contribution to the parity-odd trispectrum by the dimension-7 operator $\sim \ddot{\pi}_c\partial_i\dot{\pi}_c A_i$ is estimated. The quartic parity-odd Lagrangian is

$$\mathcal{L}_{4,\mathrm{PO}} \sim \frac{1}{\bar{\Lambda}^6}\ddot{\pi}_c\partial_i\dot{\pi}_c[\mathcal{D}_{\mathrm{PO}}^{-1}]_{ij}\ddot{\pi}_c\partial_j\dot{\pi}_c. \tag{B1}$$

Substituting $\partial_i/a \sim H/c_s$, $\ddot{\pi}_c \sim c_s^{-\frac{3}{2}}H^3$, $\dot{\pi}_c \sim c_s^{-\frac{3}{2}}H^2$, and using eq. (52), eq. (B1) becomes

$$\mathcal{L}_{4,\mathrm{PO}} \sim \frac{1}{\bar{\Lambda}^6}c_s^{-6}H^{10}\frac{\alpha_\kappa}{(1+\alpha_m^2)^2 + 4\alpha_\kappa^2}. \tag{B2}$$

The size of the parity-odd signal induced is estimated to be

$$\tau_{\mathrm{PO}}^{\ddot{\pi}_c\partial_i\dot{\pi}_c A_i} \sim \frac{\mathcal{L}_{4,\mathrm{PO}}}{c_s^{-3}H^4}\Delta_\zeta^{-2}$$
$$= c_s^{-3}\left(\frac{H}{\bar{\Lambda}}\right)^6 \frac{\alpha_\kappa\Delta_\zeta^{-2}}{(1+\alpha_m^2)^2 + 4\alpha_\kappa^2}. \tag{B3}$$

Supplemented with the perturbativity bound in eq. (34c), eq. (B3) turns into

$$\tau_{\mathrm{PO}}^{\ddot{\pi}_c\partial_i\dot{\pi}_c A_i} \sim c_s\alpha_k\Delta_\zeta^{-2} = \mathcal{O}(10^6). \tag{B4}$$

Comparing with eq. (56), the sizes of the parity-odd trispectrum contributed by the two dimension-7 operators have the same order.

[1] S. Jazayeri, S. Renaux-Petel, X. Tong, D. Werth, and Y. Zhu, Physical Review D **108**, 123523 (2023).

[2] O. H. E. Philcox, Phys. Rev. D **106**, 063501 (2022).

[3] J. Hou, Z. Slepian, and R. N. Cahn, Monthly Notices of the Royal Astronomical Society **522**, 5701 (2023).

[4] C. S. Wu, E. Ambler, R. W. Hayward, D. D. Hoppes, and R. P. Hudson, Phys. Rev. **105**, 1413 (1957).

[5] A. D. Sakharov, in *In The Intermissions... Collected Works on Research into the Essentials of Theoretical Physics in Russian Federal Nuclear Center, Arzamas-16* (World Scientific, 1998) pp. 84–87.

[6] O. H. Philcox and Z. Slepian, Proceedings of the National Academy of Sciences **119**, e2111366119 (2022).

[7] M. Shiraishi, C. Hikage, R. Namba, T. Namikawa, and M. Hazumi, Phys. Rev. D **94**, 043506 (2016).

[8] D. Jeong and M. Kamionkowski, Phys. Rev. Lett. **108**, 251301 (2012).

[9] T. Liu, X. Tong, Y. Wang, and Z.-Z. Xianyu, Journal of High Energy Physics **2020**, 1 (2020).

[10] G. Cabass, S. Jazayeri, E. Pajer, and D. Stefanyszyn, Journal of High Energy Physics **2023**, 1 (2023).

[11] D. J. Eisenstein, D. H. Weinberg, E. Agol, *et al.*, The Astronomical Journal **142**, 72 (2011).

[12] Y. Wang, Communications in Theoretical Physics **62**, 109 (2014).

[13] P. Ade, N. Aghanim, M. Arnaud, M. Ashdown, J. Aumont, C. Baccigalupi, A. Banday, R. Barreiro, J. Bartlett, *et al.*, A13 **16**, 10.1051/0004-6361/201525830 (2016).

[14] G. Hinshaw, D. Larson, E. Komatsu, D. N. Spergel, C. Bennett, J. Dunkley, M. Nolta, M. Halpern, R. Hill, N. Odegard, *et al.*, The Astrophysical Journal Supplement Series **208**, 19 (2013).

[15] O. H. E. Philcox, Physics Division Seminar, Presentation (2021), Lawrence Berkeley National Laboratory (LBNL).

[16] R. N. Cahn, Z. Slepian, and J. Hou, A Test for Cosmological Parity Violation Using the 3D Distribution of Galaxies (2021), arXiv:2110.12004 [astro-ph.CO].

[17] I. Szapudi and A. S. Szalay, The Astrophysical Journal **494**, L41 (1998).

[18] S. D. Landy and A. S. Szalay, Astrophysical Journal, Part 1 (ISSN 0004-637X), vol. 412, no. 1, p. 64-71. **412**, 64 (1993).

[19] X. Niu, M. H. Rahat, K. Srinivasan, and W. Xue, Journal of Cosmology and Astroparticle Physics **2023** (05), 018.

[20] E. T. Whittaker, Proc. Lond. Math. Soc **1**, 367 (1904).

[21] J. Goldstone, A. Salam, and S. Weinberg, Physical Review **127**, 965 (1962).

[22] D. Green, K. Gupta, and Y. Huang, arXiv preprint arXiv:2403.05274 10.48550/arXiv.2403.05274 (2024).

[23] C. Cheung, A. L. Fitzpatrick, J. Kaplan, L. Senatore, and P. Creminelli, Journal of High Energy Physics **2008**, 014 (2008).

[24] S. Jazayeri and S. Renaux-Petel, Journal of High Energy Physics **2022**, 1 (2022).

[25] A. Falkowski, Lecture notes for Saclay (2017).

[26] Z. Zhang, Journal of High Energy Physics **2017**, 1 (2017).

[27] Y. Akrami, F. Arroja, M. Ashdown, J. Aumont, C. Baccigalupi, M. Ballardini, A. Banday, R. Barreiro, N. Bartolo, S. Basak, *et al.*, Astronomy & Astrophysics **641**, A9 (2020).

[28] X. Chen, Y. Wang, and Z.-Z. Xianyu, Journal of Cosmology and Astroparticle Physics **2017** (12), 006.

[29] S. Alam, F. D. Albareti, C. A. Prieto, *et al.*, The Astrophysical Journal Supplement Series **219**, 12 (2015).

[30] K. L. Masters, C. Maraston, R. C. Nichol, D. Thomas, A. Beifiori, K. Bundy, E. M. Edmondson, T. D. Higgs, A. Leauthaud, R. Mandelbaum, *et al.*, Monthly Notices of the Royal Astronomical Society **418**, 1055 (2011).

[31] H. A. Feldman, N. Kaiser, and J. A. Peacock, The Astrophysical Journal **426**, 23 (1994).

[32] O. H. Philcox and J. Ereza, arXiv preprint arXiv:2401.09523 https://doi.org/10.48550/arXiv.2401.09523 (2024).

[33] J. Ereza, F. Prada, A. Klypin, *et al.*, arXiv preprint arXiv:2311.14456 https://doi.org/10.48550/arXiv.2311.14456 (2023).

[34] F.-S. Kitaura, S. Rodriguez-Torres, C.-H. Chuang, *et al.*, Monthly Notices of the Royal Astronomical Society **456**, 4156 (2016).

[35] P. Paul, C. Clarkson, and R. Maartens, arXiv preprint arXiv:2402.16478 https://doi.org/10.48550/arXiv.2402.16478 (2024).

[36] D. Collaboration, A. Aghamousa, J. Aguilar, S. Ahlen, *et al.*, The DESI Experiment Part I: Science, Targeting, and Survey Design (2016), arXiv:1611.00036 [astro-ph.IM].

[37] R. Laureijs, J. Amiaux, S. Arduini, *et al.*, Euclid Definition Study Report (2011), arXiv:1110.3193 [astro-ph.CO].

[38] L. S. Collaboration, P. A. Abell, J. Allison, S. F. Anderson, *et al.*, LSST Science Book, Version 2.0 (2009), arXiv:0912.0201 [astro-ph.IM].